

RESEARCH ARTICLE

Control of Movement

## A novel biomechanical model of the proximal mouse forelimb predicts muscle activity in optimal control simulations of reaching movements

✉ Jesse I. Gilmer,<sup>1</sup> ✉ Susan K. Coltman,<sup>5</sup> Geraldine Cuenu,<sup>2</sup> ✉ John R. Hutchinson,<sup>4</sup> Daniel Huber,<sup>2</sup>  
✉ Abigail L. Person,<sup>3</sup> and Mazen Al Borno<sup>1</sup>

<sup>1</sup>Department of Computer Science and Engineering, Computational Bioscience Program, University of Colorado Denver | Anschutz Medical Campus, Denver, Colorado, United States; <sup>2</sup>Department of Basic Neuroscience, University of Geneva, Geneva, Switzerland; <sup>3</sup>Department of Physiology and Biophysics, University of Colorado Denver | Anschutz Medical Campus, Denver, Colorado, United States; <sup>4</sup>Department of Comparative Biomedical Sciences, Royal Veterinary College, London, United Kingdom; and <sup>5</sup>Department of Kinesiology, The Pennsylvania State University, University Park, Pennsylvania, United States

### Abstract

Mice are key model organisms in neuroscience and motor systems physiology. Fine motor control tasks performed by mice have become widely used in assaying neural and biophysical motor system mechanisms. Although fine motor tasks provide useful insights into behaviors that require complex multi-joint motor control, there is no previously developed physiological biomechanical model of the adult mouse forelimb available for estimating kinematics, muscle activity, or kinetics during behaviors. Here, we developed a musculoskeletal model based on high-resolution imaging of the mouse forelimb that includes muscles spanning the neck, trunk, shoulder, and limbs. Physics-based optimal control simulations of the forelimb model were used to estimate *in vivo* muscle activity present when constrained to the tracked kinematics during reaching movements. The activity of a subset of muscles was recorded and used to assess the accuracy of the muscle patterning in simulation. We found that the synthesized muscle patterning in the forelimb model had a strong resemblance to empirical muscle patterning, suggesting that our model has utility in providing a realistic set of estimated muscle excitations over time when given a kinematic template. The strength of the similarity between empirical muscle activity and optimal control predictions increases as mice performance improves throughout learning of the reaching task. Our computational tools are available as open-source in the OpenSim physics and modeling platform. Our model can enhance research into limb control across broad research topics and can inform analyses of motor learning, muscle synergies, neural patterning, and behavioral research that would otherwise be inaccessible.

**NEW & NOTEWORTHY** Investigations into motor planning and execution lack an accurate and complete model of the forelimb, which could bolster or expand on findings. We sought to construct such a model using high-detail scans of murine anatomy and prior research into muscle physiology. We then used the model to predict muscle excitations in a set of reaching movements and found that it provided accurate estimations and provided insight into an optimal-control framework of motor learning.

biophysical models; motor control; muscle patterning; optimal control; reaching behaviors

### INTRODUCTION

*Mus musculus* (Mice) are key model organisms for behavioral studies in neuroscience and physiology, including for tasks that assay fine motor control and motor learning. Mice can perform tasks such as manipulandum control (1), dexterous reach (2–8), and can learn complex behaviors with and

without training (9–13). Mice are a useful organism for studying human disease, and their behaviors reflect an evolutionarily preserved trait applicable to human motor disorders (14). They also convey a benefit to researchers because of their accessible genetics and a slate of powerful molecular tools, which can allow researchers to perturb neural behavior through optogenetics (15).



Correspondence: M. Al Borno (mazen.alborno@ucdenver.edu).

Submitted 25 October 2024 / Revised 19 November 2024 / Accepted 4 March 2025



However, despite the utility of mice as a model organism in motor learning, there are no high-resolution reconstructions of the adult mouse forelimb, nor are there any physiological biomechanical models of the mouse forelimb that incorporate fully developed muscle morphology. Biomechanical models are useful tools for motor systems and neuromechanics researchers that can provide detailed insights into muscle activity and limb kinematics (e.g., fiber length and velocities) that would otherwise be difficult or impossible to access through empirical observations. State-of-the-art recording methods can only measure the activity of 3–4 muscles of the 25+ muscles in the murine forelimb (16, 17). Therefore, we set out to construct and evaluate a model of the mouse forelimb, which would be a valuable tool for researchers studying dexterous behaviors in mice.

The only currently available mouse forelimb model, developed recently in a full-body mouse model (18), was based on mouse embryo data (19), and lacks many of the large muscles originating from the scapula. Ramalingasetty et al. (18) reported that modeling the mouse forelimb was challenging and identified improving their forelimb model as a remaining challenge for future work. Moreover, reference books on limb anatomy present two-dimensional (2-D) illustrations of the limb musculature (20–22), which makes it challenging to extract accurate locations of the attachment points and the three-dimensional (3-D) tissue paths from these references (19). Attachment points have been shown to be the most important factor in estimating how effective a muscle is in producing a joint rotation or moment (23). Computing these quantities directly from dissections is challenging because of the size of the forelimb muscles, whose tendon insertion points are separated by as little as tens of microns.

We were able to more accurately identify the muscle attachment sites and muscle paths than previously possible using mouse and rat atlas data through the use of light sheet microscopy. Building on the detailed description of muscle anatomy integrated into a hindlimb biomechanical model by Charles et al. (23), we aimed to extend this work by developing a similar model for the forelimb using imaging data. We started by scanning and recreating the forelimbs of two adult mice. Muscles with insertions onto the humerus originate from sites that span most of the mouse's trunk and spine, necessitating imaging of much of the mouse body. We limited our reconstruction to muscles that had insertions onto the humerus, radius, and ulna, as reconstruction of muscles with insertions onto the scapula and those that inserted onto the hand was infeasible given the resolution of imaging performed. Once the muscles had been traced and reconstructed, they were used to construct the musculoskeletal geometry of the biomechanical model, including attachments and lines of action, using the OpenSim modeling and physics simulation environment (24–26). We used published results on mouse forelimb muscle architecture to set the muscle parameters (27). With a model based on highly accurate reconstructions and mouse physiology, we then hypothesized that our model would be well suited to the prediction of muscle activity during motor behaviors such as skilled reaching.

To evaluate the utility of the model, we then aimed to replicate physiological kinematics and predict simultaneously recorded muscle activity. We analyzed a subset of a data set

comprising thousands of reaches from three mice, which included both 3-D kinematics and the activity of a subset of muscles involved in the reaching movements [biceps, triceps long head, and triceps lateral head electromyography (EMG)]. The empirical kinematics were used as constraints when producing muscle-driven synthesized kinematics with optimal control in OpenSim. The empirical EMG was then used as a ground truth for comparison against the optimal control EMG predictions produced in simulation.

We found that optimal control-based simulations using the model were able to recreate reach kinematics accurately using synthesized muscle excitations. When examined against empirical EMG, synthetic EMG closely resembled the mean activation during kinematically matched reaches. These results suggest that our model is capable of replicating realistic reach kinematics and muscle activity. In addition, we had access to behavioral data that spanned the extent of learning, thus we performed analyses that reveal that the optimal control solutions are closer to the empirical solutions (i.e., the patterns used by real mice) as reaching performance improves throughout learning. In other words, mice may use muscle patterning solutions that more closely resemble optimal control solutions as they become more skilled at the task.

More broadly, this model should provide insight into forelimb behaviors that would otherwise be inaccessible by experimental means, and we hope that access to a robust description of the forelimb's kinematics, forces, and muscle activity will advance understanding of mouse behavior. Our computational tools are available as open-source for researchers interested in analyzing muscle activity during mouse forelimb movements.

## METHODS

### Animals

All procedures followed National Institutes of Health Guidelines and were approved by the Institutional Animal Care and Use Committee at the University of Colorado Anschutz Medical Campus under Protocol No. 43. Animals were housed in an environmentally controlled room, kept on a 12-h light-dark cycle and had ad libitum access to food and water, except during behavioral training and testing as described later. Adult C57BL/6 (Charles River Laboratories) mice of either sex (3 females and 1 male) were used in behavioral experiments. The animals for the light sheet imaging were part of experiments approved by the Animal Care Committee of the University of Geneva and by the veterinary office of the “Direction générale de la santé” of the Canton of Geneva. Adult C57BL/6 mice of the female sex (2 females) were used in imaging experiments.

### Anatomical High-Resolution Imaging

Accurate prediction of muscle activity during movements is predicated on a sufficient description of the underlying anatomy and physiology. With the goal of creating a predictive model, we began by collecting anatomical data. We obtained 3-D scans of mouse forelimbs and trunk musculature through large scale light sheet microscopy imaging of two wild-type female mice (11 wk old). The data set contains

imaging that captured the left distal shoulder and proximal forelimb (*mouse A*), the right distal forelimb and paw (*mouse A*), and both forelimbs, shoulders, and trunk (*mouse B*). Only the left shoulder, trunk, and proximal forelimb were reconstructed in *mouse B*. *Mouse A* and *B* are different from the four mice used in the empirical reaching data set with EMG. This imaging data set provides detailed anatomical information to inform our model development.

### Mouse and Tissue Preparation

Mice were euthanized via subcutaneous injection of pentobarbital. Transcardial perfusion with saline, followed by 4% paraformaldehyde (PFA) and 0.01% heparin, was performed to preserve tissue integrity. The circulatory system was then washed with saline solution, and the skin was removed. To clear the entire mice, a chamber was set up in the manner that the whole bodies were immersed under the solution that was perfused in a closed loop through the vascular system using a peristaltic pump. All the following incubation steps were performed through this perfusion setup. The bone structures of the mice were decalcified by incubating them in 20% EDTA at 37°C for 10 days, with the EDTA solution being renewed every 3 days.

Imaging subjects were pretreated with methanol following the principle of iDISCO+ tissue clearing protocol (28–30). The tissue was introduced to a gradually increasing concentration of methanol, starting with 20% and increasing by 20% every hour. The clearing chamber was maintained at room temperature. After 5 h of exposure to methanol, the tissue was chilled at 4°C overnight and then bathed in 66% dichloromethane (DCM) and 33% methanol for 24 h. The tissue was then bathed twice in 100% methanol for 1 h before being chilled for 1 h at 4°C and then transferred into 5% hydrogen peroxide in methanol for 48 h. Finally, tissue was rehydrated through 1 h immersion in 80%/60%/40%/20% methanol for 1 h per 20% decrement, then transferred to 1× PBS for 24 h, followed by immersion in a 100 mL of PBS 10× and 2 mL TritonX-100 solution that was filled to 1 L with distillate water. Since only the tissue autofluorescence was targeted for imaging, no antibodies were used in this clearing step process. The tissue was permeabilized with a solution (500 mL) consisting of 400 mL PTx.2, 11.5 g glycine, and 100 mL dimethylsulfoxide (DMSO). The tissue was bathed in solution for 4 days, then transferred to a blocking solution of 42 mL PTx.2 (100:2 solution of PBS10x:TritonX-100), 3 mL donkey serum, and 5 mL DMSO for 3 days. Finally, tissue was washed with 100 mL PBS 10×, 2 mL Tween-20, 1 mL of 10 mg/mL heparin, and filled to 1 L with distillate water. The tissue was then re-dehydrated through preparation in 20%/40%/60%/80%/100% methanol in 1 h steps, then bathed in 100% methanol overnight. Afterward, the tissue was bathed in 66% DCM and 33% methanol for 4 h, then in 100% DCM for 15 min twice, in succession, and finally immersed in dibenzyl ether (Sigma 108014-1KG) solution for imaging.

### Imaging Parameters

Dissected mouse limbs were arranged in a prone position before imaging. Scans were taken with 8.23 μm per pixel scans at ×8 zoom, with 5 μm steps in the z-plane. Imaging was performed using mesoSPIM (31). Immunostaining was

captured in the green channel (488 nm laser) and was imaged using mode tiling wizard with an offset by 75% and a filter set to 530/43. *Mouse A*'s forearms were dissected and imaged in their entirety. *Mouse B* was imaged from the base of the skull through the joint of the femur and tibia and the entirety of the depth of the sample.

### Anatomical Segmentation and Reconstruction

Muscle segments were manually reconstructed in 3-D. We found that muscle density and striation was a sufficient marker of muscles to identify them with light sheet microscopy using the tissue autofluorescence imaged in the green channel. We used imaging of the mouse anatomy and segmented individual muscles into 3-D shape objects using 3-D Slicer (32) (Fig. 1A). We also segmented the forelimb bones to obtain landmarks and geometries for use in the model. Because not every data set had complete data for the entire forelimb, right and left anatomical datasets were combined through manual alignment in Blender (33). We used anatomical landmarks on the humerus, ulna, and radius to align muscle reconstructions, as these bones were present in all three imagining datasets (left and right forelimbs of *mouse A*, and whole body of *mouse B* using the left forelimb). The reconstructions were scaled according to the radius of the bones and confirmed visually by examining the degree of overlap between reconstructions.

### Development of a Biomechanical Model of the Mouse Forelimb

With a detailed set of reconstructions, we next sought to leverage anatomical descriptions to construct a biomechanical model in OpenSim, a widely used physics-based modeling and simulation environment used to study movements of humans and other species. The anatomical model was assembled using OpenSim Creator (26). Each individual muscle's parameters were derived from optical measurements and from previous parameters in the study by Mathewson et al. (27) and Charles et al. (23). These were used to set the biophysical properties of the modeled muscles. We used De Groote et al.'s (34) Hill-type muscles within the model, and opted to ignore complex tendon dynamics (i.e., using rigid tendons with no force-length/velocity properties), both to facilitate the production of a functional model and because we did not have access to sufficient data regarding tendon physiology purely from imaging data. Our Hill-type muscles were parametrized by four parameters (maximum isometric force, optimal fiber length, tendon slack length, and pennation angle). All these parameters, except for tendon slack length, were determined experimentally in the muscle dissection study of Mathewson et al. (27) and through interpolation from known values when a muscle was not described in prior literature [i.e., for muscles with unknown physiological cross-sectional area (PSCA) values, estimates were performed through the length to PSCA relationship described by Mathewson et al. (27)]. The tendon slack length parameter represents the length where a tendon develops passive elastic force (35); this parameter cannot be measured through imaging alone and was set using the optimization procedure of Buchanan et al. (36), as is commonly performed in the field (23), assuming that muscle fibers

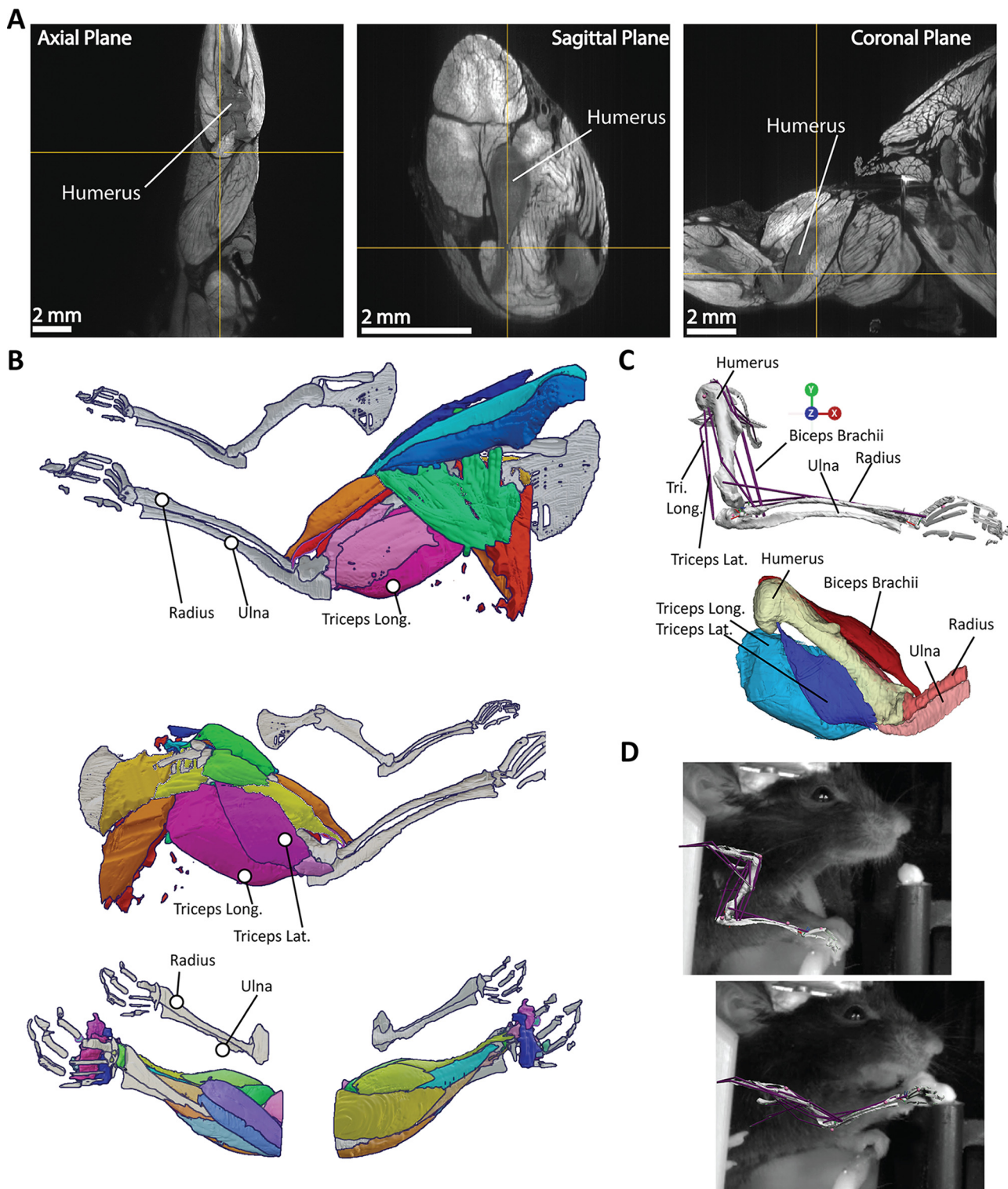


**Figure 1.** Anatomical reconstruction. **A:** optical slices of the mouse forelimb in the axial, sagittal, and coronal planes. The mouse arm is oriented in the prone position. Labels added to highlight prominent muscles as an example of a reconstruction target. **B:** three-dimensional (3-D) projections of optical tracing results as a composite across mice. Top shows composite scan, whereas bottom shows the left hand of mouse A to highlight density of wrist-inserting muscles. Three-dimensional (3-D) projections show morphology and attachment sites of muscles on bones that were used to create biophysical model. **C:** biomechanical model (OpenSim) reconstruction developed from the 3-D projections. **D:** biomechanical model projection on video images taken from a mouse reaching.

remain within 0.5 to 1.5 times optimal fiber length throughout the joint's range of motion, which were estimated from both anatomical constraints and video of mouse behavior. Based on the muscle paths from the digital segmentation, we used wrapping surfaces, which are geometric objects in OpenSim, to constrain the muscles to have realistic paths of action. This is necessary for the model to produce realistic moment arms (23). We set other parameters in the muscles such as the maximum contraction velocity, the activation time constants, and the force-length curves scaled based on prior work on mouse physiology (23, see our open-source model for details). We calculated the physiological cross-sectional area (PCSA) by the standard formula developed by Alexander and Vernon (37), that is, muscle volume divided by fiber length. Muscle fiber pennation angle is set separately in OpenSim models; thus not directly used in PCSA calculations. Bone volume was determined in reconstruction and was uniformly multiplied by a murine bone density scalar (0.00425 kg/cm<sup>3</sup>), determined from a literature search for empirical measures (38) and prior models of the mouse (23), and estimations of the center-of-mass and inertia. The resulting model has 21 muscles and five bones (along with a composite hand body segment), with the scapula and clavicle serving as fixed position bodies. The model includes four degrees-of-freedom: shoulder elevation, extension, and rotation, and elbow flexion. The model is also capable of wrist flexion and rotation, but these degrees-of-freedom were fixed during our simulations. A description of the model geometry is available in Table 1 and the muscle parameterization in Table 2.

### Model Scaling

Individual mice have variable limb dimensions that models must be altered to accommodate. We accomplished this by using the scale tool in OpenSim to automatically scale the mass, length, and muscle parameters of the model to fit the observed kinematic data originating from a particular mouse subject. We used DeepLabCut (39) to estimate paw, elbow, and shoulder markers from video. Our scripts adjusted the marker

positions based on a 3-D skeletal model with estimated limb lengths (derived from mean intermarker distances). These adjusted marker positions were then used to scale the OpenSim model to the mouse's proportions.

### Surgery for Electromyography and Behavioral Recordings

Mice underwent two surgeries, ranging 5–7 days apart. Mice were sedated with a subcutaneous ketamine/xylazine mixture (10 µL/g) and a local subcutaneous injection of bupivacaine was delivered at incision sites (80 µL at scalp, 30 µL at forearm). Surgical sites were cleared of hair and sanitized with betadine before incision. Animals were monitored during surgery for wakefulness and breathing rate, and an injection of one-third of the original sedative was used to maintain sedation as needed. Surgical sites were wetted with saline to prevent drying. Rimadyl was injected 24 and 48 h subperitoneally postsurgery to reduce discomfort (3.33 µL/g). Enrofloxacin and saline were injected subcutaneously at the same time (10 mg/kg enrofloxacin, 10 µL/g saline) to prevent injection and promote hydration. Mice were positioned in a stereotaxic apparatus (with bite bar and head bars) for the duration of surgery to maintain a flat skull bearing.

First, a head plate was attached to the mouse's cranium with Metabond dental cement. This was done to enable head fixation during the experimental training and testing. After recovery, a second surgery to implant the EMG arrays was performed. The EMG array connector was attached to the headplate with Metabond dental cement, and the connecting wires were tunneled beneath the skin of the arm to an incision site on the proximal forelimb between the biceps and triceps on the dorsal surface of the arm. A detailed surgical protocol is available on request. The leads of the MyoMatrix arrays (Part No. RF-4x8-BVS-5; 16, 17) were implanted into the biceps, triceps long head, and triceps lateral head using microsurgical needles and attached suture to secure the lead. The incision site was closed with Ethicon VICRYL 4-0 suture secured at the knot point with Gluture.

**Table 1.** Muscle origins and insertions

Muscle Name	Origin Parent-Body	Origin Coordinates, m	Insertion Parent-Body	Insertion Coordinates, m
Anconeus	Humerus	(5.2e-3, 5e-4, 1.07e-2)	Ulna	(2.4e-3, -2e-4, 8.8e-3)
Anconeus, short head	Humerus	(3.6e-3, -9e-4, 9.1e-3)	Ulna	(3.8e-3, -6e-4, 8.3e-3)
Biceps, long head	Scapula	(8.5e-3, 2.3e-2, 1.2e-2)	Ulna	(2.1e-3, 4.9e-5, 8.8e-3)
Biceps, short head	Humerus	(9.1e-3, 1.5e-3, 1.2e-2)	Ulna	(2.1e-3, 9.8e-5, 8.8e-3)
Brachialis, proximal head	Humerus	(2.3e-3, 5.9e-5, 8.8e-3)	Ulna	(2.2e-3, 5.9e-5, 8.8e-3)
Brachialis, distal head	Humerus	(8.2e-3, 1.4e-3, 1.2e-2)	Ulna	(2.2e-3, 5.9e-5, 8.8e-3)
Brachioradialis	Humerus	(4e-3, 6.5e-4, 9.1e-3)	Radius	(-3e-3, 1.3e-3, 1.2e-2)
Deltoid, medial	Clavicle	(9.3e-3, 5e-4, 1.3e-2)	Humerus	(5.5e-3, 1.2e-3, 1.2e-2)
Deltoid, posterior	Scapula	(8.7e-3, 1.2e-3, 1.2e-2)	Humerus	(5.9e-3, 1.5e-3, 1.1e-2)
Flexor carpi radialis	Humerus	(3.4e-3, -9.3e-4, 9.2e-3)	Hand	(-4e-3, 1.6e-3, 1.2e-2)
Infraspinatus	Scapula	(1.1e-2, 1.3e-3, 1.2e-2)	Humerus	(8.3e-3, 1.6e-3, 1.2e-2)
Latissimus dorsi, caudal	Spine*	(1.8e-2, -3e-3, 1e-2)	Humerus	(5.5e-3, 1.7e-3, 1.1e-2)
Latissimus dorsi, rostral	Spine*	(1.5e-2, -7.1e-4, 1.3e-2)	Humerus	(5.9e-3, 1.5e-3, 1.1e-2)
Pectoralis major, anterior	Rib-cage*	(9.1e-3, -1.6e-3, 1.7e-2)	Humerus	(5.3e-3, 1.4e-3, 1.2e-2)
Pectoralis major, posterior	Rib-cage*	(1e-2, -3.1e-3, 1.5e-2)	Humerus	(5.5e-3, 1.6e-3, 1.2e-2)
Pectoralis minor, clavicular	Clavicle	(1.1e-2, -9.6e-4, 1.3e-2)	Humerus	(5.6e-3, 1.2e-3, 1.2e-2)
Pronator teres	Humerus	(3.6e-3, -6.7e-4, 9.3e-3)	Radius	(8.8e-4, 1.2e-3, 1e-2)
Subscapularis	Scapula	(1.3e-2, 4e-4, 1.3e-2)	Humerus	(8.2e-3, 6.2e-4, 1.2e-2)
Triceps, long head	Scapula	(9.8e-3, 1.2e-3, 1.2e-2)	Ulna	(4.2e-3, -5.7e-4, 8e-3)
Triceps, lateral head	Humerus	(8.4e-3, 1.6e-3, 1.2e-2)	Ulna	(4.1e-3, -4.5e-4, 8.3e-3)
Triceps, medial head	Humerus	(6.5e-3, 2.5e-4, 1.1e-2)	Ulna	(3.8e-3, -2.3e-4, 8.4e-3)

\*Spinal and rib attachments made to Scapula fixed ground object.

**Table 2.** Muscle parameters

Muscle Name	Max Isometric Force, N	Optimal Fiber Length, m	Pennation Angle, rad	Tendon Slack Length, m
Anconeus	0.023	0.003	0.1	0.0002
Anconeus, short head	0.02	0.0015	0.1	0.00015
Biceps, long head	0.093	0.0085	0.1	0.0002
Biceps, short head	0.018	0.005	0.1	0.0005
Brachialis, proximal head	0.066	0.007	0.1	0.0001
Brachialis, distal head	0.067	0.007	0.1	0.0001
Brachioradialis	0.02	0.007	0.1	0.0001
Deltoid, medial	0.069	0.006	0.2	0.0002
Deltoid, posterior	0.068	0.0035	0.2	0.0001
Flexor carpi radialis	0.02	0.007	0.1	0.0001
Infraspinatus	0.065	0.003	0.2	0.0001
Latissimus dorsi, caudal	0.133	0.011	0.36	0.0005
Latissimus dorsi, rostral	0.1133	0.011	0.36	0.0005
Pectoralis major, anterior	0.233	0.008	0.3	0.0002
Pectoralis major, posterior	0.170	0.007	0.3	0.0005
Pectoralis minor, clavicular	0.033	0.0056	0.25	0.0002
Pronator teres	0.02	0.003	0.1	0.0001
Subscapularis	0.34	0.005	0.2	0.0001
Triceps, long head	0.612	0.008	0.3	0.0007
Triceps, lateral head	0.125	0.007	0.17	0.0001
Triceps, medial head	0.16	0.004	0.2	0.0001

### Behavioral Training and Recording

Mice were placed on the experimental rig 5–7 days post-EMG implant in a headfix standing position, with forepaws on a thin bar. Postsurgery, mice were maintained at 80%–85% of their initial body weight throughout training and testing phases to encourage feeding behavior. During data collection, mice were head-fixed on the experimental rig and trained to perform a single pellet retrieval task (Fig. 1*D* and Fig. 2*A*) and allowed to retrieve anywhere from 10 to 50 pellets (BioServe Dustless Precision Pellets F0163). Kinematic measurements and EMG recordings were continuously collected throughout the entire training process, starting from the first session when the mice were completely naive until they gradually improved and achieved expertise in the task. This training period spanned 11 to 26 sessions, with the mice making their first successful reach (i.e., retrieving a pellet) between 2 to 5 sessions on the rig.

We collected EMG data from the biceps brachii, triceps long head, and triceps lateral head in four mice. Muscle activity was measured simultaneously with MyoMatrix arrays (16, 17), using a bipolar INTAN RHD Recording Headstage (Intan Part No. C3232, RHD 16-channel bipolar + accelerometer) and captured by an Open Ephys system (40), at 25,000 Hz. Mouse reaching behavior was recorded from two cameras, spaced 60° apart (recorded at 150 Hz using two FLIR Blackfly S model BFS-U3-16S2M-CS cameras) with one camera capturing behavior in profile, and one rostral to the animal's resting position.

### Kinematic Reconstruction

Recorded behaviors were processed using the DeepLabCut 3-D motion tracking software (39). Postprocessing of the data parsed the recorded movements into reaching movements, which included the position of the shoulder, elbow, wrist, and paw. Although prior studies have captured scapular motion (41, 42), we were unable to accurately distinguish movement above the scapulohumeral joint in our video

recordings. We estimated the elbow joint angle from the 3-D markers. We used the average limb lengths to adjust the DeepLabCut paw, elbow, and shoulder markers and ensure that the limb lengths remain constant throughout the video, which is necessary for accurate tracking by the model. Because our forelimb model only has rotational degrees-of-freedom on the shoulder, we could not capture the small translational movement occurring at the shoulder during head-fixed reaching. We subtracted the shoulder markers displacements from the elbow and paw markers to keep shoulder positional coordinates fixed in our simulations.

### EMG Postprocessing

We band-pass filtered the recorded EMG signals from 5 to 500 Hz, rectified the signal, then low-passed further with a cutoff of 10 Hz (Supplemental Fig. S2). Processed EMG envelopes were normalized to the maximum contraction recording during the session. EMG is usually normalized to the maximum voluntary contractions in studies with human subjects (43), and comparison to the inherently normalized activity in our model necessitated this step. Each muscle was recorded through 4 leads, but only the qualitatively determined cleanest lead per muscle was used for this study.

### Selection of Reaches for Simulation

Our data set spanned the entirety of reach training for four mice, and because of the progression of learning, there was natural variance in kinematics performed. We opted to select only from “expert” mice and to use baseline EMG datasets that were derived from similar reaching kinematics, which eliminated one of the mice. We grouped reaches using the 2-norm metric on 3-D paw kinematics to assess similarity, and then selected two sets of 10 reaches per mice ( $n = 3$ ), with each set having a different kinematic profile (see Fig. 2*C*). We enforced expertise by selecting reaches that occurred only after the initial four sessions of learning, which was a typical epoch for mice to reach moderate success in reaching. We also compared the optimal control predictions between the early and

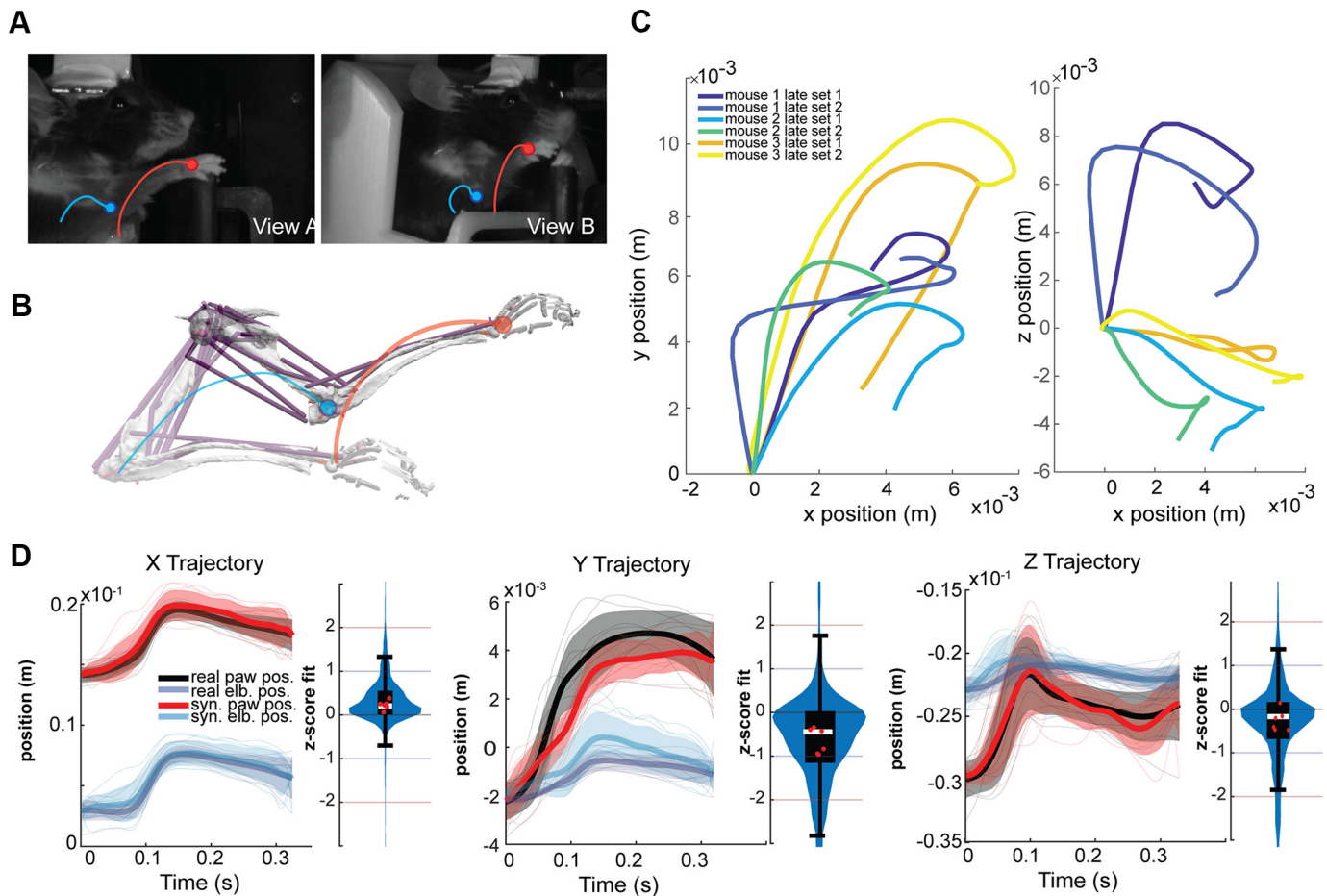


**Figure 2.** *A:* example video screenshots with schematic elbow and paw marker trajectories. *B:* a biomechanical model with virtual markers on the elbow and paw. An optimal control problem is solved to minimize the difference between the virtual and empirical markers (See Supplemental Video 1 for an example of the model in motion with muscle activations visualized). *C:* means of six sets of reaches selected for simulation, with the  $x$  vs.  $y$  (forward vs. vertical) dimensions plotted on the *left* and  $x$  vs.  $z$  (forward vs. lateral) on the *right*. Blue and purple trajectories originate from *mouse 1*, green and teal from *mouse 2*, and orange and yellow from *mouse 3*. See Supplemental Videos S2–S7 for paw trajectory comparisons in motion. *D:* an example of real and synthetic reach kinematic comparisons for *mouse 3*, along with computed mean and standard deviation of all 60 reaches analyzed (20/mouse, 10 per set) for the empirical and synthesized marker trajectories (black boxplots within blue violins). The  $z$ -score of the synthesized markers is largely within 1 standard deviation (see violin plots in blue), and the means per set of ten reaches are all within 1 standard deviation (red dots). Black box plots denote median (white bar), 25 to 75th percentile distributions (black box), and 10th to 90th percentile distributions (short horizontal black lines).

late sessions of learning. Early sessions were selected from the four mice discussed earlier (i.e., including the mouse that did not achieve expertise status). Ten reaches were selected from each mouse for the early data set. Early sessions were restricted to the first three sessions of learned reaching.

#### Optimal Control

Optimization of synthetic movements matching empirical kinematics was conducted with direct collocation in Moco (44) as it is well-suited for simulations that track experimental data ('inverse simulations'; e.g., see Ref. 45). Direct collocation enforces the equations-of-motion and physiological relationships as constraints in a nonlinear optimization problem that solves for the states of the musculoskeletal system and the muscle activity over the duration of the simulation. The optimization's objective is to minimize a cost function of two terms: one term that is a proxy for effort (i.e., the sum of muscle activations squared) and one term that represents the tracking cost (i.e., the deviation between the

synthesized and the experimental kinematics). The cost function equation is:

$$E = wT_{\text{paw}} + wT_{\text{elbow}} + \sum_i a_i^2$$

Here,  $T_{\text{paw}}$  is the 2-norm squared difference between model and experimental 3-D paw coordinates. The experimental coordinates comprised of 100 timepoints during the ballistic phase of reaching (starting with initiation of movement, e.g., deviation from resting, containing peak outward velocity, and including 15 ms following peak achievement of outward reaching position). The same holds for  $T_{\text{elbow}}$ , which is derived from tracking of the mouse elbow position. Term  $a_i$  denotes the activation of muscle  $i$  in the model and  $w$  is a scalar weight set to  $10^9$ . We optimized over 2,500 iterations and 100 mesh points. The simulation was also constrained to start with the joint angles derived during the scaling of the model. The optimization would end early if a convergence tolerance of  $1e^{-7}$  was reached. The optimization typically ran for 10 min on a

computer with specifications listed in Supplemental Table S1. Rarely, MoCo would not resolve an appropriate kinematic solution for muscle-driven simulations (in 2 trials), in which case the cost function was altered to  $w = 10^{12}$  then resimulated with a template guess taken from the set.

We compared range normalized predicted muscle activity and EMG measurements using the mean absolute error (MAE) metric at an optimal lag (in a range of -50 to +10 ms; we used a lag of 0 ms for Fig. 3 and the late reach set in Fig. 4; early reaches had an optimal lag of -50 ms in Fig. 4).

### Analysis of Model Utility

To determine whether the synthetic muscle excitations produced by the model provided insight into physiological activity, we compared the fit of the synthetic data to the mean muscle activity per set of 10 reaches (6 sets total). Although we would ideally compare on a per-reach basis, we found that inherent variability in muscle excitation in the physiological data made single-reach matching difficult (Supplemental Fig. S1). We instead asked whether the synthetic data was more informative than knowing the baseline distribution of the physiological activity by comparing synthetic data to time-shuffled physiological data (Fig. 3C). Data were randomized across time using a `randperm()` function of the time index in MATLAB. Fit to physiological mean was then computed and the mean absolute errors were compared using a bidirectional *t* test. Time indexes were restricted to match those simulated by the model.

When comparing the early and late simulation datasets, we found that individual muscle excitation fits were not significant. To assess whether there was a gross change in goodness of fit, we pooled muscle fits across biceps, triceps long head, and triceps lateral head into a single comparison, which is reflected in Fig. 4.

## RESULTS

### Kinematic Tracking

We tasked the physiological forelimb model to track recorded DeepLabCut-tracked kinematics using optimal control algorithms (see *Optimal Control*). The model was scaled and then optimized with direct collocation to track the paw and elbow across the ballistic epoch of the reach (Fig. 2, A and B; encapsulating the initiation of movement through peak outward velocity, and terminating 15 ms after achieving peak outward position). Animals have natural variance in produced reaching movements and motor control, so we opted to group six sets of 10 reaches by their kinematic similarity across time (Fig. 2C; see *Selection of Reaches for Simulation*). We deliberately selected these sets of varying reaching kinematics to explore the ability of the model to predict varied motor behaviors. We were able to recreate limb kinematics with low error, with the majority of synthesized kinematics per timestep falling within 1 standard deviation of the empirical kinematic mean (Fig. 2D, blue violin plots;  $n = 60$  reaches) across the  $x$ ,  $y$ , and  $z$  dimensions of the paw and elbow trajectories (here,  $x$  is forward,  $y$  is upward, and  $z$  is lateral displacement when viewing motion from a profile view with respect to the mouse).

### Model Muscle Activity Patterning for Reaching Movements

We next tasked the model to synthesize muscle activity during reaching movements with optimal control to predict the muscle excitations that underlie observed kinematics. The predictions were not trained with “ground truth” or empirical muscle activity. As shown in the examples in Fig. 3A, we observed that the mean synthesized muscle activity closely resembles empirical muscle activity over the duration of the reach for all three muscles. We measured the performance of the model via the mean absolute error (MAE) of normalized ground truth EMG signals from model signals. The mean muscle excitations produced by the model were typically within a single standard deviation of the experimental EMG activity (Fig. 3B, red dots in violin plots; between 50 and 57 of the 60 reaches, depending on the mice and assayed muscle).

On a reach-by-reach basis, the muscle excitations produced by the model across all time points were typically within two standard deviations of the experimental EMG activity, suggesting that, while still relatively accurate, individual reaches are more difficult to accurately predict. Paired reach-to-reach predictions were likely less accurate because mice were highly variable in their muscle patterning, even between reaches with the same kinematic profile (Supplemental Fig. S1). Some of the observed muscle patterning may be energetically inefficient, more consistent with early learning or motor exploration, which would not be predicted as accurately by optimal control approaches. In Fig. 3C, we show that the mean model EMG predictions outperformed the shuffled experimental EMG data (i.e., having the same distribution as the ground truth EMG; two-sided *t* test, biceps  $P = 6.4\text{e-}7$ , triceps long head  $P = 1.5\text{e-}6$ , triceps lateral head  $P = 6.2\text{e-}3$ ; *P* values were Holm–Bonferroni corrected for multiple comparisons,  $n = 60$  shuffled trials and six synthesized means).

### Mouse Motor Learning and Optimal Control

The progression of reach kinematics and muscle patterning in mice learning a novel task is a relatively understudied phenomenon, especially given the paucity of experimental approaches to studying whole limb muscle activity. We leveraged our model’s explanatory power to investigate the possibility that mice approach an optimal motor control solution during the progression of training by evaluating optimal control predictions during early and late sessions of training. In Fig. 3, we compared the optimal control predictions with reaches selected from expert mice (i.e., after at least 5 sessions of successful reaching). In Fig. 4, we compared how the optimal control predictions varied when the reaches were chosen in the early (i.e., in the first 3 sessions after the first successful reach to pellet) or late stages of learning. We found that mice tended to use muscle excitation patterns that converged more closely to those derived from optimal control in the later stages of learning. These results were significant when pooling the data across all recorded EMG channels but not on individual channels, likely because of our small sample size (early  $n = 4$ , late  $n = 6$  for means comparisons, early  $n = 40$ , late  $n = 60$  for trial-to-trial comparisons shown in Fig. 4. Comparison of trial-to-trial data was compared with a two-sided *t* test with a *P* value of  $2.4\text{e-}5$ ).

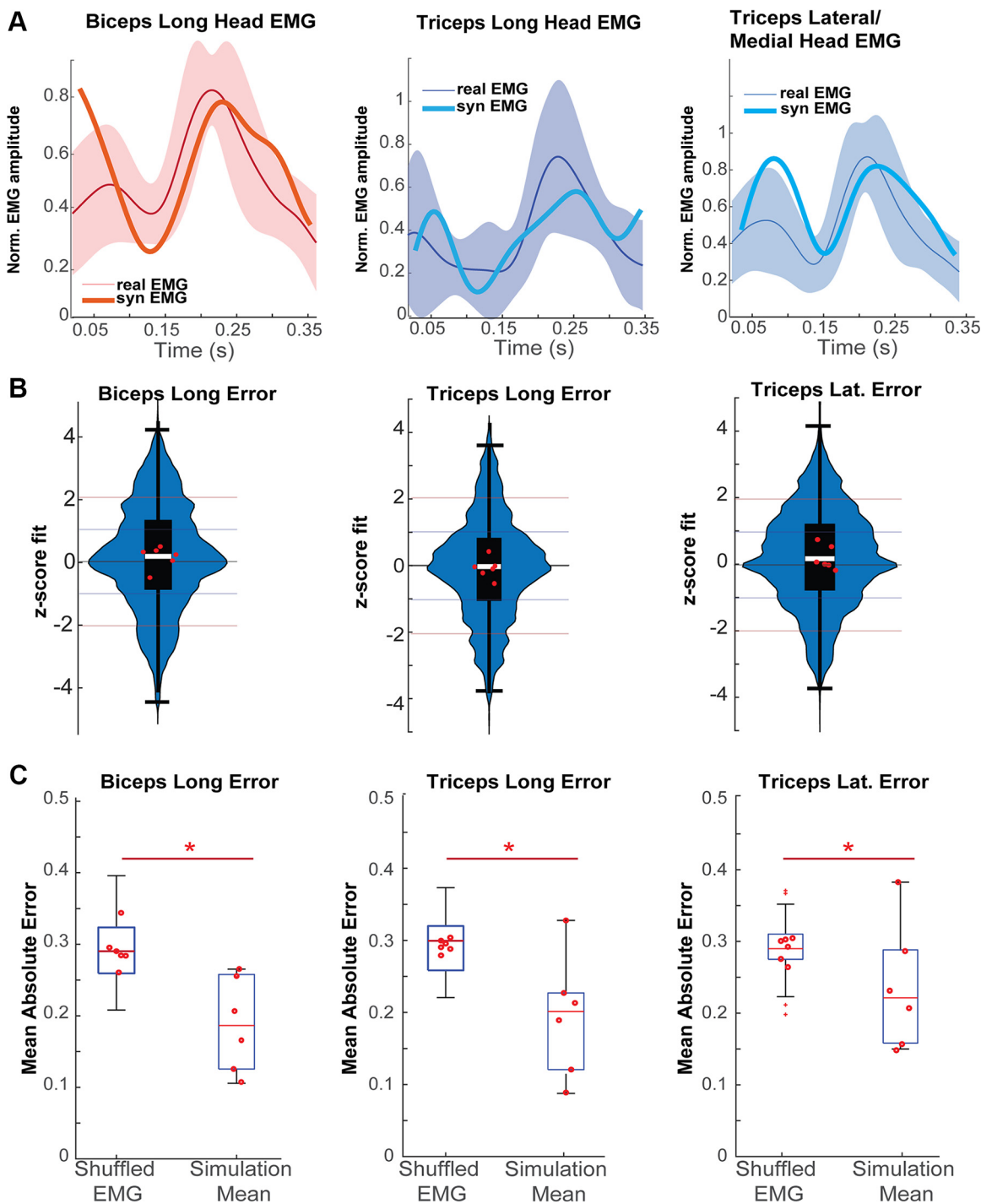


**Figure 3.** A: comparisons of synthesized muscle excitations and experimental electromyography (EMG) activity. Curves show means and standard deviations (line and shaded region) of 10 reaches with similar experimental elbow and paw trajectories that were chosen from mouse behavior dataset. The mean synthesized excitations are shown in thick red for biceps long head, thick cyan for triceps long head, and thick blue for triceps medial head compared with the base lateral head activity. B: violin plots including the entire dataset of 60 reaches. The mean synthesized muscle activity lies largely within 1 standard deviation of mean experimental muscle activity (red dots). On a reach-by-reach basis, the synthesized muscle activity lies largely within a z-score of 2 standard deviations (blue violin plots). Black box plots denote median z-deviation (white bar), 25 to 75th percentile distributions (black box), and 10th to 90th percentile distributions (horizontal black line). C: a comparison of mean absolute error between time-shuffled physiological EMG data and synthetic excitation means to the real mean of the tracked data. Synthetic excitation means have lower mean absolute error (MAE) than the time-shuffled data in all three muscles recorded (two-sided *t* test, biceps  $P = 6.4\text{e-}7$ , triceps long head  $P = 1.5\text{e-}6$ , triceps lateral head  $P = 6.2\text{e-}3$ . \**P* values were Holm–Bonferroni corrected for multiple comparisons). Black box plots denote median (red horizontal bar), 25 to 75th percentile distributions (black box), and 10th to 90th percentile distributions (short horizontal black lines and stems).

## Bulk EMG Prediction

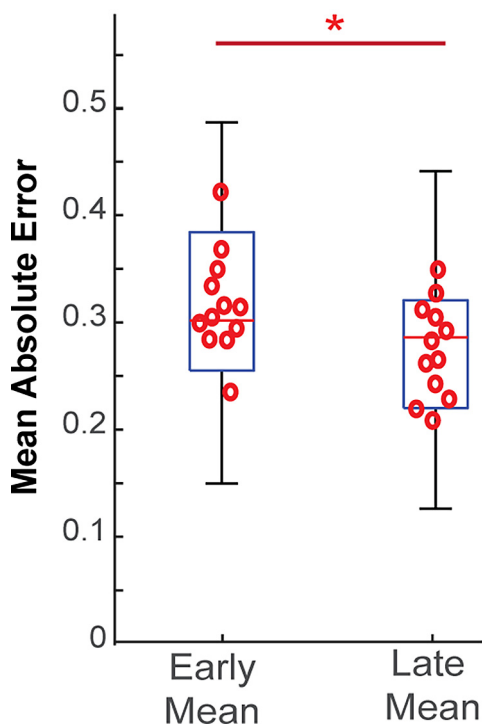


**Figure 4.** A comparison of the utility of the simulated muscle excitations in predicting electromyography (EMG) during early or late training sessions (i.e., the first three sessions after the first successful reaches being early and sessions later than four sessions after the initial successful reach being late.). Late reaches, on bulk, have a significantly lower mean absolute error than early sessions (two-sided  $t$  test,  $P = 2.4e-5$ , early  $n = 40$ , late  $n = 60$ , \*Significant) for predicting trial-to-trial EMG activity. Black box plots denote median (red horizontal bar), 25 to 75th percentile distributions (black box), and 10th to 90th percentile distributions (short horizontal black lines and stems).

## DISCUSSION

Mouse models are widely used to study the neural control of movement, motor disorders, muscle physiology, and develop novel brain-computer interfaces and neurotechnologies. Despite the widespread use of mice in the health sciences, the only available biomechanical model of the mouse forelimb is based largely on educated guesses, which could lead to inaccurate kinematics and muscle activity predictions. We used high-detail anatomical reconstruction from large-scale light sheet microscopy scans to develop one of the first physiological biomechanical model of the mouse forelimb in terms of musculoskeletal geometry and muscle architecture (27). This manuscript was published in tandem with a similar model developed by DeWolf et al. (46), which used micro-computer tomography (CT) to develop a two-armed murine model. Though there is some disagreement in terms of muscle insertion locales between our study and the DeWolf model, it remains to be seen how much impact subtle variations in modeled anatomy has on predicting physiological muscle excitation patterning, and will likely be the subject of ongoing research. Traditional dissection methods were deemed impractical to determine the musculoskeletal geometry because of the small size of the mouse

forelimb, especially in determining the attachment points of the tendons of the elbow. We used this biomechanical model with optimal control to synthesize muscle coordination patterns that produce reaching movements in simulations that match experimental kinematics. Accurately predicting muscle activity is challenging because of the infinite possible coordination patterns consistent with the tracked experimental kinematics and the high physiological variance in the patterns observed in real mice (i.e., for very similar kinematics, mice often use very different muscle patterning strategies, some of which may be energetically costly, have high or low cocontraction, be robust to disturbances, etc.; Supplemental Fig. S1) and in human studies [Feldotto et al. (47)]. Our optimal control cost function only has terms to encourage low energy (via the sum of muscle activations squared proxy) and producing kinematics consistent with experimental kinematics. Therefore, we would not expect the optimal control predictions to closely match the experimental muscle activity on a reach-by-reach basis because of the high variability in the experimental muscle patterning data. Nevertheless, we found that the mean optimal control muscle activity predictions have a strong resemblance with the mean empirical muscle activity (Fig. 3A). These results held for all three recorded muscles with EMG (biceps, triceps long head, and triceps lateral head). To the best of our knowledge, this is among the earliest works in any species, including humans [though see Feldotto et al. (47) for similar results in leg movements], showing a resemblance between synthesized and experimental muscle activity for three-dimensional reaching movements with a biomechanical model.

Neuroscience experiments are sometimes limited in scope by the difficulty of simultaneous recording of behavior, neurological signals, and, in some cases, muscle activity. Multisite muscle recordings are limited to accessible sites, and this limitation is exacerbated in mice, where access to and implantation of many muscles is often infeasible. This model is meant to supplement experiments where knowledge of muscle activity patterning could bring insight about the nature of neural activity patterning. Scientists with behavioral data can extract an estimate of whole forelimb muscle activity from the model given a set of kinematics over time. Tracking of mouse kinematics has become broadly accessible through the advent of pose-based tracking software like DeepLabCut, which was used in the present study to monitor limb position during reaching behaviors (39). The conjunction of tracking and synthesis of whole forelimb muscle activations promises to expand research into behavioral control significantly.

There are several extensions to our biomechanical model and computational tools possible for future work. Our computational tools assume that no EMG is available during the experiments. If EMG is collected during the experiment, the optimal control problem can be solved to predict the muscle activity of muscles without EMG recordings while matching experimental EMG and kinematics data in tracking simulations (44). It is also possible to change the cost function in the optimal control problem and produce predictive simulations that do not require any experimental data, including kinematics, by specifying goals constrained only to endpoint or end-state of the limb. The optimal control problem could then predict the reaching kinematics and muscle activity when there is a change in the task (e.g., a new pellet

location) or limb biomechanics (e.g., a weight placed on the forelimb). This model might also be used to assay disease states to expand on known motor symptoms, such as enforced variability in end point accuracy as seen in cerebellar disease (48), impaired kinematics in Parkinson's disease (49), and for assaying kinematic impairments in stroke victims, such as forced variation in muscle coordination patterns (41, 42, 50). Analysis of specific motor coordination patterns in murine models of disease has heretofore been impossible to fully measure. Although this model's utility in describing disease states will require validation, the opportunity to fully describe the state of the forelimb may grant insight into muscle patterning and synergies that were previously not described and may suggest rehabilitative activities that act on impacted motor structures (51).

Although the model evaluation in this study focuses on reaching movements, which are commonly used to assess motor control across species, the insights gained extend beyond this specific task. Reaching movements provide a well-studied framework for understanding motor coordination, but motor systems are capable of generating numerous possible muscle coordination patterns for any given movement (52). Optimal control chooses the muscle excitation pattern that achieves task constraints while minimizing a proxy for effort or energy (e.g., the sum of muscle activations squared) and possibly other terms (53). We apply optimal control to predict an energetically efficient muscle activity pattern that achieves the reaching kinematics task. This study is focused on the ballistic phase of reaching movements, and we did not model the grasping phase during the reach as we would have needed to include the muscles that control the wrist and fingers in the model and simulate interaction with the pellet. One additional discrepancy between our simulation and the empirical reach is that mice, before starting their reach, rested their paws on a bar, which we did not simulate (and may impact the predicted muscle activity at the start of the ballistic phase, see Fig. 3A biceps for an example of elevated EMG activity likely generated to offset gravity not present in the physiological experiment).

Our simulations were evaluated with head-fixed mouse reaching. Using the biomechanical model in free-reaching mice may be less accurate because it has more significant scapular movements, which we assume to stay fixed in our model, but which can be measured (42). In future work, researchers could either add a degree-of-freedom and a joint motor to allow translational movement of the scapula or incorporate the muscles that control the scapula as a free body in the biomechanical model. The optimal control solutions produce open-loop muscle coordination patterns that are not responsive to noise or changing task or environmental constraints. It is, however, possible to develop closed-loop controllers to track the optimized trajectory or to develop feedback controllers with reinforcement learning or introduce stochastic noise representing imprecise neural controls (e.g., see Ref. 54). Finally, we generalized our muscle parameterization to past work and observations from other small mammals (55), but the model would certainly benefit from a thorough investigation of the murine forelimb's muscles through dissection and testing, which was beyond the scope of our study.

We make our computational tools freely available as open-source. We have written custom code to convert our OpenSim model into the MuJoCo physics simulation environment (56) included in the project repository at SimTK.org. Although the model is available in MuJoCo, the computational tools for optimal control are based in OpenSim; therefore, MuJoCo users will need to develop their own code to produce the simulations with the model. Although the model evaluation in this study focuses on reaching movements, our tools can be used to predict muscle activity in other forelimb movements. Users of our computational tools should note that the optimal control predictions are expected to more closely resemble empirical muscle activity on a mean basis rather than on a trial-by-trial basis and carry the assumption of closely matched kinematics. Furthermore, the model predictions are expected to improve when mice have learned to perform the task well as opposed to when mice are still in the early stages of learning. Nevertheless, the model predictions in the early stages of learning are still within one standard deviation of empirical results and represent a significant improvement over randomized guesses from the naturalistic EMG distribution. An exciting use case for our biomechanical model is to control it with artificial neural networks and relate the activity in these networks with empirical neural activity from system neuroscience laboratories (57). We have also provided our anatomical data and reconstructions on Zenodo (see DATA AVAILABILITY), which contain a number of distal forelimb muscles whose attachment points were too minute to clearly identify, but which may be of interest to researchers examining dexterous movement of the wrist and fingers. Combining our computational tools and experimental data could lay the foundations for future studies elucidating the principles that drive the control of movement.

## DATA AVAILABILITY

The OpenSim model and scripting tools used in the study are available at [https://simtk.org/projects/mouse\\_arm2024](https://simtk.org/projects/mouse_arm2024). The anatomical imaging and reconstruction files are available at <https://zenodo.org/records/14206069>.

## SUPPLEMENTAL MATERIAL

Supplemental Figs. S1 and S2, Supplemental Table S1, and Supplemental Videos S2–S7: <https://doi.org/10.18735/sayr-8m76>.

## ACKNOWLEDGMENTS

We thank InWorks at CU Denver for imaging and segmentation.

## GRANTS

The behavioral study included in this work was supported by NIH Grants (along with Simons Consortium): U24NS126936 and R01NS109237. J.I.G. was supported by NLM Grants 2T15LM009451-16 and 5T15LM009451-15.

## DISCLOSURES

No conflicts of interest, financial or otherwise, are declared by the authors.

## AUTHOR CONTRIBUTIONS

J.I.G., S.K.C., G.C., D.H., A.L.P., and M.A.B. conceived and designed research; J.I.G., S.K.C., and G.C. performed experiments; J.I.G. and M.A.B. analyzed data; J.I.G., J.R.H., and M.A.B. interpreted results of experiments; J.I.G. prepared figures; J.I.G. and M.A.B. drafted manuscript; J.I.G., S.K.C., G.C., J.R.H., D.H., A.L.P., and M.A.B. edited and revised manuscript; J.I.G. and M.A.B. approved final version of manuscript.

## REFERENCES

- Bolu T, Whitehead SC, Prasad N, Walker J, Shyamkumar N, Subramaniam R, Kardon B, Cohen I, Goldberg JH. Automated home cage training of mice in a hold-still center-out reach task. *J Neurophysiol* 121: 500–512, 2019. doi:[10.1152/jn.00667.2018](https://doi.org/10.1152/jn.00667.2018).
- Becker MI, Calame DJ, Wrobel J, Person AL. Online control of reach accuracy in mice. *J Neurophysiol* 124: 1637–1655, 2020. doi:[10.1152/jn.00324.2020](https://doi.org/10.1152/jn.00324.2020).
- Becker MI, Person AL. Cerebellar control of reach kinematics for endpoint precision. *Neuron* 103: 335–348.e5, 2019. doi:[10.1016/j.neuron.2019.05.007](https://doi.org/10.1016/j.neuron.2019.05.007).
- Calame DJ, Becker MI, Person AL. Cerebellar associative learning underlies skilled reach adaptation. *Nat Neurosci* 26: 1068–1079, 2023. doi:[10.1038/s41593-023-01347-y](https://doi.org/10.1038/s41593-023-01347-y).
- Fleischer P, Abbasi A, Fealy AW, Danielsen NP, Sandhu R, Raj PR, Gulati T. Emergent low-frequency activity in cortico-cerebellar networks with motor skill learning. *Eneuro* 10: ENEURO.0011-23, 2023. doi:[10.1523/ENEURO.0011-23.2023](https://doi.org/10.1523/ENEURO.0011-23.2023).
- Khanna P, Totten D, Novik L, Roberts J, Morecraft RJ, Ganguly K. Low-frequency stimulation enhances ensemble co-firing and dexterity after stroke. *Cell* 184: 912–930.e20, 2021. doi:[10.1016/j.cell.2021.01.023](https://doi.org/10.1016/j.cell.2021.01.023).
- Yang W, Kanodia H, Arber S. Structural and functional map for forelimb movement phases between cortex and medulla. *Cell* 186: 162–177.e18, 2023. doi:[10.1016/j.cell.2022.12.009](https://doi.org/10.1016/j.cell.2022.12.009).
- Wagner MJ, Kim TH, Kadmon J, Nguyen ND, Ganguli S, Schnitzer MJ, Luo L. Shared cortex-cerebellum dynamics in the execution and learning of a motor task. *Cell* 177: 669–682.e24, 2019. doi:[10.1016/j.cell.2019.02.019](https://doi.org/10.1016/j.cell.2019.02.019).
- Burgess CP, Lak A, Steinmetz NA, Zatka-Haas P, Bai Reddy C, Jacobs EAK, Linden JF, Paton JJ, Ranson A, Schröder S, Soares S, Wells MJ, Wool LE, Harris KD, Carandini M. High-yield methods for accurate two-alternative visual psychophysics in head-fixed mice. *Cell Rep* 20: 2513–2524, 2017. doi:[10.1016/j.celrep.2017.08.047](https://doi.org/10.1016/j.celrep.2017.08.047).
- Serradj N, Marino F, Moreno-López Y, Bernstein A, Agger S, Soliman M, Sloan A, Hollis E. Task-specific modulation of corticospinal neuron activity during motor learning in mice. *Nat Commun* 14: 2708, 2023. doi:[10.1038/s41467-023-38418-4](https://doi.org/10.1038/s41467-023-38418-4).
- Sauerbrei BA, Guo J-Z, Cohen JD, Mischiati M, Guo W, Kabra M, Verma N, Mensh B, Branson K, Hantman AW. Cortical pattern generation during dexterous movement is input-driven. *Nature* 577: 386–391, 2020. doi:[10.1038/s41586-019-1869-9](https://doi.org/10.1038/s41586-019-1869-9).
- Galiñanes GL, Bonardi C, Huber D. Directional reaching for water as a cortex-dependent behavioral framework for mice. *Cell Rep* 22: 2767–2783, 2018. doi:[10.1016/j.celrep.2018.02.042](https://doi.org/10.1016/j.celrep.2018.02.042).
- Conner JM, Bohannon A, Igarashi M, Taniguchi J, Baltar N, Azim E. Modulation of tactile feedback for the execution of dexterous movement. *Science* 374: 316–323, 2021. doi:[10.1126/science.abh1123](https://doi.org/10.1126/science.abh1123).
- Iwaniuk AN, Whishaw IQ. On the origin of skilled forelimb movements. *Trends Neurosci* 23: 372–376, 2000. doi:[10.1016/S0166-2236\(00\)01618-0](https://doi.org/10.1016/S0166-2236(00)01618-0).
- Deisseroth K, Feng G, Majewska AK, Miesenböck G, Ting A, Schnitzer MJ. Next-generation optical technologies for illuminating genetically targeted brain circuits. *J Neurosci* 26: 10380–10386, 2006. doi:[10.1523/JNEUROSCI.3863-06.2006](https://doi.org/10.1523/JNEUROSCI.3863-06.2006).
- Zia M, Chung B, Sober S, Bakir MS. Flexible multielectrode arrays with 2-D and 3-D contacts for in vivo electromyography recording. *IEEE Trans Compon Packaging Manuf Technol* 10: 197–202, 2020. doi:[10.1109/TCMPM.2019.2963556](https://doi.org/10.1109/TCMPM.2019.2963556).
- Chung B, Zia M, Thomas KA, Michaels JA, Jacob A, Pack A et al. Myomatrix arrays for high-definition muscle recording. *eLife* 12: RP88551, 2023. doi:[10.7554/eLife.88551](https://doi.org/10.7554/eLife.88551).
- Ramalingasetty ST, Danner SM, Arreguit J, Markin SN, Rodarie D, Kathe C, Courtine G, Rybak IA, Ijspeert AJ. A whole-body musculoskeletal model of the mouse. *IEEE Access* 9: 163861–163881, 2021. doi:[10.1109/access.2021.3133078](https://doi.org/10.1109/access.2021.3133078).
- DeLaurier A, Burton N, Bennett M, Baldock R, Davidson D, Mohun TJ, Logan MP. The Mouse Limb Anatomy Atlas: an interactive 3D tool for studying embryonic limb patterning. *BMC Dev Biol* 8: 83, 2008. doi:[10.1186/1471-213X-8-83](https://doi.org/10.1186/1471-213X-8-83).
- Hebel R, Stromberg MW. *Anatomy and Embryology of the Laboratory Rat*. BioMed Verl, 1986.
- Dogdas B, Stout D, Chatziloannou AF, Leahy RM. Digimouse: a 3D whole body mouse atlas from CT and cryosection data. *Phys Med Biol* 52: 577–587, 2007. doi:[10.1088/0031-9155/52/3/003](https://doi.org/10.1088/0031-9155/52/3/003).
- Navarro M, Ruberte J, Carretero A. Myology. In: *Morphological Mouse Phenotyping*, edited by Ruberte J, Carretero A, Navarro M. Academic Press, 2017, p. 63–88. doi:[10.1016/B978-0-12-812972-2.50004-0](https://doi.org/10.1016/B978-0-12-812972-2.50004-0).
- Charles JP, Cappellari O, Spence AJ, Hutchinson JR, Wells DJ. Musculoskeletal geometry, muscle architecture and functional specialisations of the mouse hindlimb. *PLoS One* 11: e0147669, 2016. doi:[10.1371/journal.pone.0147669](https://doi.org/10.1371/journal.pone.0147669).
- Delp SL, Anderson FC, Arnold AS, Loan P, Habib A, John CT, Guendelman E, Thelen DG. OpenSim: open-source software to create and analyze dynamic simulations of movement. *IEEE Trans Biomed Eng* 54: 1940–1950, 2007. doi:[10.1109/TBME.2007.901024](https://doi.org/10.1109/TBME.2007.901024).
- Seth A, Hicks JL, Uchida TK, Habib A, Dembia CL, Dunne JJ, Ong CF, DeMers MS, Rajagopal A, Millard M, Hamner SR, Arnold EM, Yong JR, Lakshminikanth SK, Sherman MA, Ku JP, Delp SL. OpenSim: simulating musculoskeletal dynamics and neuromuscular control to study human and animal movement. *PLoS Comput Biol* 14: e1006223, 2018. doi:[10.1371/journal.pcbi.1006223](https://doi.org/10.1371/journal.pcbi.1006223).
- Kewley A, Beesel J, Seth A. OpenSim Creator (Version 0.5.12). Zenodo, 2024. doi:[10.5281/ZENODO.11086325](https://doi.org/10.5281/ZENODO.11086325).
- Mathewson MA, Chapman MA, Hentzen ER, Fridén J, Lieber RL. Anatomical, architectural, and biochemical diversity of the murine forelimb muscles. *J Anat* 221: 443–451, 2012. doi:[10.1111/j.1469-7580.2012.01559.x](https://doi.org/10.1111/j.1469-7580.2012.01559.x).
- Branch A, Tward D, Kolstad AC, Pulyadi V, Vogelstein JT, Wu Z, Gallagher M. An optimized tissue clearing protocol for rat brain labeling, imaging, and high throughput analysis (Preprint). *bioRxiv*, 2019. doi:[10.1101/639674](https://doi.org/10.1101/639674).
- Renier N, Wu Z, Simon DJ, Yang J, Ariel P, Tessier-Lavigne M. iDISCO: a simple, rapid method to immunolabel large tissue samples for volume imaging. *Cell* 159: 896–910, 2014. doi:[10.1016/j.cell.2014.10.010](https://doi.org/10.1016/j.cell.2014.10.010).
- Habart M, Lio G, Soumier A, Demilly C, Sirigu A. An optimized iDISCO + protocol for tissue clearing and 3D analysis of oxytocin and vasopressin cell network in the developing mouse brain. *STAR Protoc* 4: 101968, 2023. doi:[10.1016/j.xpro.2022.101968](https://doi.org/10.1016/j.xpro.2022.101968).
- Voigt FF, Kirschenbaum D, Platонova E, Pagès S, Campbell RAA, Kastli R, Schaettlin M, Egolf L, van der Bourg A, Bethge P, Haenraets K, Frézel N, Topilko T, Perin P, Hillier D, Hildebrandt S, Schueth A, Roebroeck A, Roska B, Stoeckli ET, Pizzala R, Renier N, Zeilhofer HU, Karayannis T, Ziegler U, Batti L, Holtmaat A, Lüscher C, Aguzzi A, Helmchen F. The mesoSPIM initiative: open-source light-sheet microscopes for imaging cleared tissue. *Nat Methods* 16: 1105–1108, 2019. doi:[10.1038/s41592-019-0554-0](https://doi.org/10.1038/s41592-019-0554-0).
- Fedorov A, Beichel R, Kalpathy-Cramer J, Finet J, Fillion-Robin J-C, Pujol S, Bauer C, Jennings D, Fennessy F, Sonka M, Buatti J, Aylward S, Miller JV, Pieper S, Kikinis R. 3D Slicer as an image computing platform for the Quantitative Imaging Network. *Magn Reson Imaging* 30: 1323–1341, 2012. doi:[10.1016/j.mri.2012.05.001](https://doi.org/10.1016/j.mri.2012.05.001).
- Blender Development Team. Blender (Version 3.2.2) (Online). <https://www.blender.org> [2025 Feb 4].
- De Groote F, Kinney AL, Rao AV, Fregly BJ. Evaluation of direct collocation optimal control problem formulations for solving the muscle redundancy problem. *Ann Biomed Eng* 44: 2922–2936, 2016. doi:[10.1007/s10439-016-1591-9](https://doi.org/10.1007/s10439-016-1591-9).
- Uchida TK, Delp S, Delp DB. *Biomechanics of Movement: The Science of Sports, Robotics, and Rehabilitation*. The MIT Press, 2021.
- Buchanan TS, Lloyd DG, Manal K, Besier TF. Neuromusculoskeletal modeling: estimation of muscle forces and joint moments and

- movements from measurements of neural command. *J Appl Biomech* 20: 367–395, 2004. doi:[10.1123/jab.20.4.367](https://doi.org/10.1123/jab.20.4.367).
37. Alexander RM, Vernon A. The dimensions of the knee and ankle muscles and the forces they exert. *J Hum Movt Stud* 1: 115–123, 1975.
  38. Robbins A, Tom CATMB, Cosman MN, Moursi C, Shipp L, Spencer TM, Brash T, Devlin MJ. Low temperature decreases bone mass in mice: implications for humans. *Am J Phys Anthropol* 167: 557–568, 2018. doi:[10.1002/ajpa.23684](https://doi.org/10.1002/ajpa.23684).
  39. Mathis A, Mamidanna P, Cury KM, Abe T, Murthy VN, Mathis MW, Bethge M. DeepLabCut: markerless pose estimation of user-defined body parts with deep learning. *Nat Neurosci* 21: 1281–1289, 2018. doi:[10.1038/s41593-018-0209-y](https://doi.org/10.1038/s41593-018-0209-y).
  40. Siegle JH, Cuevas López A, Patel YA, Abramov K, Ohayon S, Voigts J. Open Ephys: an open-source, plugin-based platform for multichannel electrophysiology. *J Neural Eng* 14: 045003, 2017. doi:[10.1088/1741-2552/aa5eea](https://doi.org/10.1088/1741-2552/aa5eea).
  41. Balbinot G, Schuch CP, Jeffers MS, McDonald MW, Livingston-Thomas JM, Corbett D. Post-stroke kinematic analysis in rats reveals similar reaching abnormalities as humans. *Sci Rep* 8: 8738, 2018. doi:[10.1038/s41598-018-27101-0](https://doi.org/10.1038/s41598-018-27101-0).
  42. Balbinot G, Denize S, Lagace DC. The emergence of stereotyped kinematic synergies when mice reach to grasp following stroke. *Neurorehabil Neural Repair* 36: 69–79, 2022. doi:[10.1177/15459683211058174](https://doi.org/10.1177/15459683211058174).
  43. Kendall FP, McCreary EK, Provance PG, Rodgers MM, Romani WA. *Muscles: Testing and Function, with Posture and Pain* (Kendall, Muscles). Lippincott Williams and Wilkins, 2005.
  44. Dembia CL, Bianco NA, Falisse A, Hicks JL, Delp SL. OpenSim Moco: musculoskeletal optimal control. *PLoS Comput Biol* 16: e1008493, 2020. doi:[10.1371/journal.pcbi.1008493](https://doi.org/10.1371/journal.pcbi.1008493).
  45. Bishop PJ, Falisse A, De Groote F, Hutchinson JR. Predictive simulations of running gait reveal a critical dynamic role for the tail in bipedal dinosaur locomotion. *Sci Adv* 7: eabi7348, 2021. doi:[10.1126/sciadv.abi7348](https://doi.org/10.1126/sciadv.abi7348).
  46. DeWolf T, Schneider S, Soubiran P, Roggenbach A, Mathis MW. Neuro-musculoskeletal modeling reveals muscle-level neural dynamics of adaptive learning in sensorimotor cortex (Preprint). *bioRxiv*, 2024. doi:[10.1101/2024.09.11.612513](https://doi.org/10.1101/2024.09.11.612513).
  47. Feldotto B, Soare C, Knoll A, Sriya P, Astill S, de Kamps M, Chakrabarty S. Evaluating muscle synergies with EMG data and physics simulation in the neurorobotics platform. *Front Neurorobot* 16: 856797, 2022. doi:[10.3389/fnbot.2022.856797](https://doi.org/10.3389/fnbot.2022.856797).
  48. Bonnefoi-Kyriacou B, Legallet E, Lee RG, Trouche E. Spatio-temporal and kinematic analysis of pointing movements performed by cerebellar patients with limb ataxia. *Exp Brain Res* 119: 460–466, 1998. doi:[10.1007/s002210050361](https://doi.org/10.1007/s002210050361).
  49. Vissani M, Palmisano C, Volkmann J, Pezzoli G, Micera S, Isaia IU, Mazzoni A. Impaired reach-to-grasp kinematics in parkinsonian patients relates to dopamine-dependent, subthalamic beta bursts. *NPJ Parkinsons Dis* 7: 53, 2021. doi:[10.1038/s41531-021-00187-6](https://doi.org/10.1038/s41531-021-00187-6).
  50. Cheung VCK, Turolla A, Agostini M, Silvoni S, Bennis C, Kasi P, Paganoni S, Bonato P, Bizzi E. Muscle synergy patterns as physiological markers of motor cortical damage. *Proc Natl Acad Sci USA* 109: 14652–14656, 2012. doi:[10.1073/pnas.1212056109](https://doi.org/10.1073/pnas.1212056109).
  51. Balbinot G, Touvykine B, Zaftis J, Schuch CP, Jeffers MS, Elgbeili G, Dancause N, Corbett D. Enriched rehabilitation reduces abnormal motor synergies and enhances motor plasticity following severe stroke in rats. *Stroke* 54: 2156–2166, 2023. doi:[10.1161/STROKEAHA.123.043053](https://doi.org/10.1161/STROKEAHA.123.043053).
  52. Harris CM, Wolpert DM. Signal-dependent noise determines motor planning. *Nature* 394: 780–784, 1998. doi:[10.1038/29528](https://doi.org/10.1038/29528).
  53. Al Borno M, Vyas S, Shenoy KV, Delp SL. High-fidelity musculoskeletal modeling reveals that motor planning variability contributes to the speed-accuracy tradeoff. *eLife* 9: e57021, 2020. doi:[10.7554/elife.57021](https://doi.org/10.7554/elife.57021).
  54. Van Wouwe T, Ting LH, De Groote F. An approximate stochastic optimal control framework to simulate nonlinear neuro-musculoskeletal models in the presence of noise. *PLoS Comput Biol* 18: e1009338, 2022. doi:[10.1371/journal.pcbi.1009338](https://doi.org/10.1371/journal.pcbi.1009338).
  55. Powell PL, Roy RR, Kanim P, Bello MA, Edgerton VR. Predictability of skeletal muscle tension from architectural determinations in guinea pig hindlimbs. *J Appl Physiol Respir Environ Exerc Physiol* 57: 1715–1721, 1984. doi:[10.1152/jappl.1984.57.6.1715](https://doi.org/10.1152/jappl.1984.57.6.1715).
  56. Todorov E, Erez T, Tassa Y. MuJoCo: a physics engine for model-based control. 2012 IEEE/RSJ International Conference on Intelligent Robots and Systems. Vilamoura-Algarve, Portugal, 2012, p. 5026–5033. doi:[10.1109/IROS.2012.6386109](https://doi.org/10.1109/IROS.2012.6386109).
  57. Aldarondo D, Merel J, Marshall JD, Hasenclever L, Klibaite U, Gellis A, Tassa Y, Wayne G, Botvinick M, Ölveczky BP. A virtual rodent predicts the structure of neural activity across behaviours. *Nature* 632: 594–602, 2024. doi:[10.1038/s41586-024-07633-4](https://doi.org/10.1038/s41586-024-07633-4).